

Physical properties of maritime low clouds as retrieved by combined use of Tropical Rainfall Measurement Mission Microwave Imager and Visible/Infrared Scanner: Algorithm

Hirohiko Masunaga,¹ Takashi Y. Nakajima,¹ Teruyuki Nakajima,² Misako Kachi,¹ Riko Oki,¹ and Shunsuke Kuroda^{2,3}

Received 13 April 2001; revised 10 August 2001; accepted 27 August 2001; published 22 May 2002.

[1] Satellite remote sensing studies on the microphysical and optical properties of clouds have constructed an active research field in the last decades. Clouds are observed over a wide spectral range from the visible/infrared to the microwave, and either shortwave or microwave measurement is used to evaluate the liquid water path (LWP). On the other hand, to date, there have been few cloud studies based on combined measurement by a visible/infrared imager and a microwave radiometer aboard the same platform. In this paper a physical inversion algorithm for the combined use of visible/infrared and microwave sensors is proposed to retrieve the cloud physical quantities such as LWP and the effective droplet radius, each of which is determined in two different ways. The current version of the algorithm has been developed for application to the Tropical Rainfall Measurement Mission (TRMM) sensors, i.e., Visible and Infrared Scanner (VIRS) and TRMM Microwave Imager (TMI). The cloud top temperature obtained from the VIRS analysis is used as an input to the TMI analysis to reduce uncertainties in estimation of LWP. Total errors in LWP are estimated to range from 11 to 30 g/m². In the algorithm the beam-filling efficiency of clouds for TMI footprints is corrected by the cloud fraction evaluated from the VIRS measurements. For application, global analysis is performed with 3-monthly data from January to March 2000. The scatter diagram of the shortwave-retrieved LWP (LWP_{shrt}) versus the microwave-retrieved LWP (LWP_{micr}) shows characteristic trends for both precipitating and nonprecipitating clouds. Vertical inhomogeneity of the cloud droplet size accounts for small excess of LWP_{shrt} over LWP_{micr} for nonprecipitating clouds, while precipitating clouds produce LWP_{micr} larger than LWP_{shrt} , owing to the presence of raindrops. These tendencies are reinforced by examination of the global distributions of the shortwave-retrieved droplet radius $R_{e(NV)}$ and the microwave counterpart defined by LWP divided by the cloud optical thickness $R_{e(MV)}$. The result implies that difference in those effective radii reflects a microphysical mechanism to expedite or suppress the conversion of the cloud water into rainfall. **INDEX TERMS:** 0320 Atmospheric Composition and Structure: Cloud physics and chemistry; 1610 Global Change: Atmosphere (0315, 0325); 1640 Global Change: Remote sensing; 1694 Global Change: Instruments and techniques; **KEYWORDS:** low clouds, effective radius, algorithm, TRMM

1. Introduction

[2] Clouds are known to play significant roles in Earth's radiation budget, and it is necessary to clarify the global characteristics of clouds for climate system studies. Investigation of the microphysical and optical properties of clouds by means of satellite remote sensing has been an important subject in the last decades. An established

¹Earth Observation Research Center, National Space Development Agency, Tokyo, Japan.

²Center for Climate System Research, University of Tokyo, Tokyo, Japan.

³Now at Sun Microsystems, Inc., Tokyo, Japan.

scheme to retrieve the effective droplet radius and the optical thickness of clouds employs a pair of shortwave channels, where combination of a water-absorbing channel in the near-infrared wavelength region and a nonabsorbing channel in the visible yields the effective droplet radius and the optical thickness through a well-behaving inversion algorithm [Nakajima and King, 1990; Han et al., 1994; Nakajima and Nakajima, 1995; Kawamoto et al., 2001]. The cloud optical thickness at an optical wavelength τ_c , along with the effective droplet radius R_e , provides the shortwave-retrieved liquid water path LWP_{shrt} of clouds according to the well-known formula

$$LWP_{\text{shrt}} = \frac{2\rho_w}{3} R_e \tau_c = \frac{2\rho_w}{3} \gamma \langle R_e \rangle \tau_c, \quad (1)$$

where R_e is defined by

$$R_e = \frac{\int_0^\infty r^3 n(r) dr}{\int_0^\infty r^2 n(r) dr} \quad (2)$$

under a given droplet size distribution $n(r)$. The mass density of liquid water ρ_w is constant at 10^6 g/m^3 . The correction factor γ , to relate the shortwave-retrieved R_e with the vertically averaged value $\langle R_e \rangle$, accounts for the vertical inhomogeneity of R_e [Nakajima and King, 1990; Brenguier et al., 2000]. If R_e increases with the altitude as typically observed in nonprecipitating cumulus clouds, γ exceeds unity because R_e retrieved from satellite remote sensing is biased toward the value near the cloud top due to the large absorption of near-infrared radiation by cloud droplets.

[3] LWP can be retrieved from microwave brightness temperatures as well as from shortwave radiances. A large number of algorithms have been developed to derive LWP over oceanic environment by means of microwave radiometers [Chang and Wilheit, 1979; Wilheit and Chang, 1980; Takeda and Liu, 1987; Petty, 1990; Greenwald et al., 1993; Lin et al., 1998a]. Comparison of the microwave-retrieved liquid water path LWP_{micr} with LWP_{shrt} obtained by spaceborne sensors has been made by some authors. Greenwald et al. [1993] confirmed at a local observation site that LWP retrieved by Special Sensor Microwave/Imager (SSM/I) measurement is consistent with that by advanced very high resolution radiometer (AVHRR). Lojou et al. [1991] improved a regression formula for LWP_{micr} using LWP_{shrt} to eliminate a bias between scanning multichannel microwave radiometer (SMMR) and visible and infrared spin-scan radiometer (VISSR) measurements. Lin and Rossow [1994] revealed that LWP_{micr} and LWP_{shrt} are in good agreement for warm nonprecipitating clouds on the basis of global analysis of SSM/I and International Satellite Cloud Climatology Project (ISCCP) data.

[4] Zuidema and Hartmann [1995] and Greenwald et al. [1995] compiled data from SSM/I, ISCCP, and the Earth Radiation Budget Experiment (ERBE) to derive LWP, cloudiness, and effective droplet radius of liquid water clouds. Combined measurements by shortwave and microwave radiometers can also be made to detect the cloud overlapping, as demonstrated by Lin et al. [1998a, 1998b] in the use of SSM/I and ISCCP retrievals.

[5] There are some difficulties with the combined use of multiple sensors onboard different satellites. One of the problems arises if the data are not matched in space and time. Furthermore, the criterion for the presence of clouds is clearly defined in the shortwave retrieval algorithms in terms of significantly larger reflectance and/or substantially lower temperature than the ground, whereas the cloud emission in the microwave is much less distinct from the surface radiation. Lin and Rossow [1994] implied that the arbitration in the cloud detection threshold is responsible for a large dispersion in LWP provided by past investigators. Microwave observations synchronized by shortwave measurement of clouds are expected to avoid such ambiguities in estimation of LWP.

[6] The difference in the spatial resolution between the shortwave and microwave radiometers is another obstacle to

comparison of LWP_{micr} and LWP_{shrt} . The typical footprint size is 1 or 2 km for shortwave imagers, while it extends up to a few tens of kilometers for passive microwave sensors. Therefore LWP_{micr} would be smoothed out within a field of view to produce significantly smaller values than LWP_{shrt} when the cloud fraction is small. The beam-filling efficiency in microwave measurement should be corrected before comparing LWP_{micr} and LWP_{shrt} .

[7] Combined use of a visible/infrared imager and a microwave radiometer onboard the same platform overcomes these difficulties. Moreover, the combined use also has the advantage that the cloud top temperature, whose uncertainty is known to produce serious errors in evaluation of LWP [Greenwald et al., 1993], is determined precisely from the visible/infrared measurement. In this paper we propose an algorithm to retrieve the cloud properties by the combined measurements. We apply our algorithm to global analysis using the Tropical Rainfall Measurement Mission (TRMM) data. The present algorithm also has potential for application to future satellite programs with multiple sensors onboard such as the Aqua project directed by NASA, Advanced Earth Observation Satellite (ADEOS) II by the National Space Development Agency of Japan (NASDA), and some future programs in planning stages.

[8] The retrieval algorithm is described and verified in section 2. In section 3 we introduce the satellite and ancillary data that are used in the analysis. Section 4 shows results of the data analysis, and conclusions are summarized in section 5.

2. Retrieval Method

[9] In this section we describe the algorithm used to derive the cloud physical properties from visible/infrared radiances and microwave brightness temperatures, which is designed for application to the TRMM data. The TRMM satellite has the Visible/Infrared Scanner (VIRS) and TRMM Microwave Imager (TMI) on board, as well as precipitation radar (PR). VIRS is an AVHRR-like imager with the five channels at the wavelengths of 0.63, 1.6, 3.75, 10.8, and 12 μm . TMI is similar to SSM/I but has two additional low-frequency channels at 10.65 GHz (V and H), 19.35 GHz (V and H), 21.3 GHz (V), 37.0 GHz (V and H), and 85.5 GHz (V and H), where V and H designate vertical and horizontal polarizations, respectively. The frequency of the water vapor channel at 21.3 GHz has been shifted from the line-centered position at 22.235 GHz as specified by SSM/I in order to avoid saturation in the tropics.

[10] The visible/infrared technique and microwave scheme for our analysis are introduced separately, followed by the description on the overall flow of the combined analysis. Table 1 summarizes the retrieved products in our algorithm.

2.1. Retrieval Scheme for Visible/Infrared Measurement

[11] Nakajima and Nakajima [1995] described a method for determining the microphysical properties of water clouds by visible and infrared measurements using AVHRR data. The original version of the Nakajima and Nakajima algorithm used a fixed water vapor profile to correct the

Table 1. Summary of the Retrieved Products^a

Sensor	Channels in Use	Retrievals	Algorithm
VIRS	0.63, 3.75, and 10.8 μm	τ_c $R_{e(\text{NV})}$ T_c LWP_{shrt}	GLI algorithm ^b
TMI	10.65 GHz (V), 19.35 GHz (V, H), and 37.0 GHz (H)	f_c CWV LWP_{micr} $R_{e(\text{MV})}$ ^c	this paper

^aDefinitions are as follows: VIRS, Visible/Infrared Scanner; GLI, Global Imager; TMI, Tropical Rainfall Measurement Mission Microwave Imager; CWV, columnar water vapor.

^bFrom *Nakajima and Nakajima* [1995] and *Kawamoto* [2001].

^cWith the help of T_c .

atmospheric component in the thermal emission, which is justified only for regional experiments. *Kawamoto et al.* [2001] improved the Nakajima and Nakajima algorithm to make it applicable to global analysis by AVHRR with the help of the objective analysis archives to evaluate the equivalent water vapor amount. The latest version of the algorithm, which has been improved in technical aspects of the numerical scheme, is incorporated in the standard analysis system for Global Imager (GLI) to be onboard the ADEOS II satellite. We adopt the latest GLI algorithm for VIRS analysis in the present work with modification due to differences in the channel specifications.

[12] The visible/infrared algorithm is briefly outlined as follows. Lookup tables are made in advance on the basis of a set of atmospheric radiative transfer simulations using the numerical scheme presented by *Nakajima and Tanaka* [1986, 1988] and *Stamnes et al.* [1988]. The optical thickness, the effective droplet radius, and the cloud top temperature are determined by the Newton-Raphson iteration from channel 1 (0.6 μm), channel 3 (3.75 μm), and channel 4 (10.8 μm) radiances. The retrieval scheme is designed to properly subtract the ground components in the channel 1 and channel 3 radiances and the thermal component in the channel 3 for the solar radiation measurement to obtain the optical thickness and the effective radius of clouds. In this procedure we simultaneously evaluate the cloud top temperature from the channel 4 brightness temperature with given ancillary data for the surface temperature, taking into account the cloud optical thickness and the water vapor correction. Although the GLI algorithm is applicable to clouds over both ocean and land, we restrict current analysis into the marine environment for the purpose of the data matching with TMI measurement. *Nakajima and Nakajima* [1995] and *Kawamoto et al.* [2001] present a more detailed description of the visible/infrared algorithm.

2.2. Retrieval Scheme for Microwave Measurement

[13] We have recently developed a numerical code for atmospheric radiative transfer to make a lookup table for microwave brightness temperatures. Fundamental strategy of the numerical scheme follows its precursor developed for visible/infrared radiative transfer [*Nakajima and Tanaka*, 1983, 1986, 1988; *Stamnes et al.*, 1988]. In order to apply the original scheme to the microwave version we have made some modifications, as described below.

[14] Microwave brightness temperature is sensitive to the variation of the atmospheric water vapor. We specify the vertical profile of the water vapor content $\text{WVC}(z)$ as

$$\text{WVC}(z) = \frac{\text{CWV}}{H_w} \exp\left(-\frac{z}{H_w}\right), \quad (3)$$

where H_w is the scale height of the water vapor profile and CWV is columnar water vapor. In our algorithm, H_w can be treated as an input parameter in the lookup table to take into account the regional variation of the water vapor profile. We tentatively set a constant value of $H_w = 2.3$ km in the present analysis. The gas absorption coefficients are from *Liebe and Layton* [1987].

[15] It is known that in oceanic environment the surface emissivity and reflectivity for microwaves vary with the near-surface wind speed through the surface roughness, coverage of foam, and diffraction effects, in addition to change in the dielectric constant of seawater depending on sea surface temperature and salinity. See *Nakajima and Tanaka* [1983] for the formalism of the surface roughness effect, substituting a value of the mean square slope $\sigma^2 = 0.00534u_{10}$ with a microwave counterpart proposed by *Wentz and Meissner* [1999]:

$$\sigma^2 = 0.00522u_{10} \quad \nu \geq 37 \text{ GHz} \\ \sigma^2 = 0.00522 \left[1 - 0.00748(37 - \nu)^{1.3} \right] u_{10} \quad \nu < 37 \text{ GHz}, \quad (4)$$

where u_{10} is wind speed (m/s) measured 10 m above the surface. The effects of sea foam and diffraction are taken into account according to the empirical formula derived by *Wentz and Meissner* [1999] with interpolation of the data table onto the TMI channel frequencies.

[16] Some authors have made use of specific combinations of brightness temperatures to reduce uncertainties in the surface emissivity originally developed for the CWV retrieval. *Chang and Wilhelm* [1979] used the ratio of $(T_{22V} - T_s)/(T_{19V} - T_s)$ for the retrieval of atmospheric parameters since it is insensitive to the surface emissivity, where T_{19V} and T_{22V} designate the brightness temperatures in vertical polarization at 19.35 and 22.235 GHz, respectively, and T_s is the surface temperature. *Prabhakara et al.* [1982] found that the brightness temperature difference between the 18- and 21-GHz channels on SMMR is useful to derive CWV because of insensitivity to the surface emissivity. *Tjemkes et al.* [1991] pointed out that both of these two methods suffer from saturation for large values of CWV and alternatively proposed a semianalytic formula in terms of the brightness temperature difference at 19.35 GHz and $(T_{19H} - \bar{T})/(T_{19V} - \bar{T})$, with \bar{T} approximated by the climatological sea surface temperature.

[17] *Greenwald et al.* [1993] derived a couple of analytic formulae to obtain CWV and LWP, extending the formulation of *Tjemkes et al.* [1991] to the 37.0-GHz brightness temperatures in addition to the 19.35-GHz brightness temperatures. They found that the largest source of error in derivation of LWP is uncertainty in the cloud temperature. *Lin et al.* [1998a] showed that the combined use of T_{37H} and T_{85V} clearly discriminates LWP from the contribution of the cloud water temperature to the brightness temperatures. They found that uncertainties in CWV are the most important sources of error in estimation of LWP.

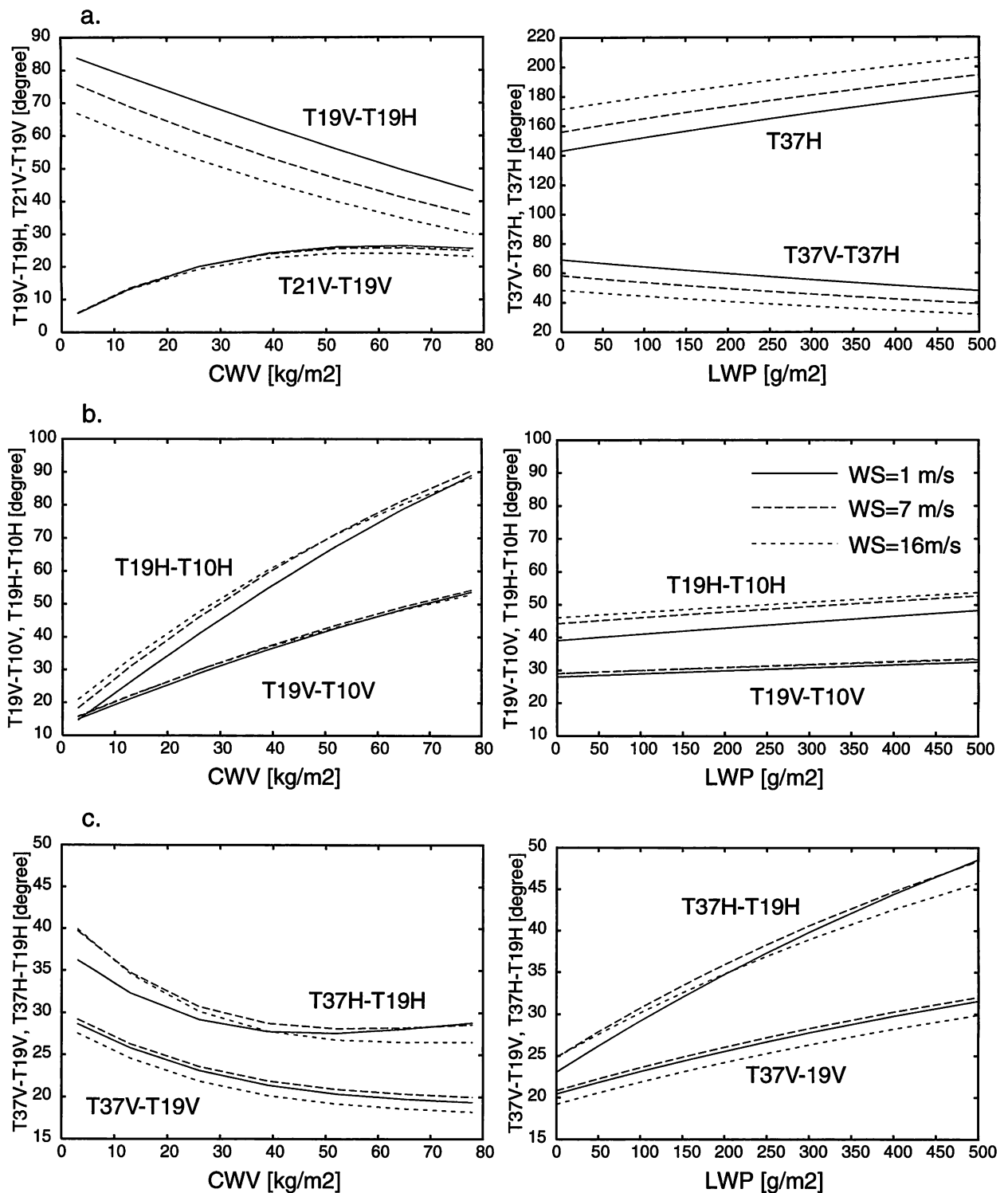


Figure 1. Calculated brightness temperatures as functions of columnar water vapor (CWV) or liquid water path (LWP). (a) $T_{21V} - T_{19V}$ and $T_{19V} - T_{19H}$ as functions of (left) CWV and $T_{37V} - T_{37H}$ and T_{37H} of as functions of (right) LWP. (b) $T_{19V} - T_{10V}$ and $T_{19H} - T_{10H}$ as functions of (left) CWV and of (right) LWP. (c) $T_{37V} - T_{19V}$ and $T_{37H} - T_{19H}$ as functions of (left) CWV and (right) of LWP. Solid, dashed, and dotted lines correspond to wind speeds (WS) of 1, 7, and 16 m/s, respectively.

[18] Our algorithm appropriately takes into account the global variation of the surface conditions such as sea surface temperature and near-surface wind speed by adopting the ancillary data (see section 3). Nevertheless, ambiguities in

the dependence on near-surface wind speed are still not negligible in estimation of LWP. Intrinsic uncertainties in near-surface wind speed are difficult to remove partly because of our limited knowledge of the dielectric proper-

ties of foam-covered water and partly because there is no global-scale validation of the archived data for near-surface wind speed.

[19] Figure 1 demonstrates the calculated brightness temperatures in various combinations to examine their sensitivities to CWV, LWP, and near-surface wind speed, where other variables are fixed as $H_w = 2$ km, sea surface temperature is 288.5 K, cloud top temperature is 282 K, and cloud base temperature is 285.25 K. Figure 1a shows some arbitrary combinations of brightness temperatures for reference. As *Tjemkes et al.* [1991] pointed out, $T_{21V} - T_{19V}$ is insensitive to the surface emissivity, and thus to near-surface wind speed but is saturated when CWV is >50 kg/m². The brightness temperature difference in a dual-polarization channel such as $T_{19V} - T_{19H}$ and $T_{37V} - T_{37H}$ is a good tracer for CWV or LWP but depends greatly on near-surface wind speed [see also *Tjemkes et al.*, 1991; *Greenwald et al.*, 1993]. A single brightness temperature such as T_{37H} also has a large dependence on both LWP and near-surface wind speed, especially in horizontal polarization.

[20] Figures 1b and 1c propose alternative combinations of brightness temperatures. The brightness temperature difference between the 19- and 10-GHz channels (ΔT_{19-10} , shown in Figure 1b) is found to have sufficiently small dependence on near-surface wind speed, in particular for the vertical polarization, without saturation over the whole realistic range of CWV. In contrast, ΔT_{19-10} is almost independent of LWP. The brightness temperature difference between the 37- and 19-GHz channels (ΔT_{37-19}) is also insensitive to near-surface wind speed with satisfactory sensitivity to LWP for the horizontal polarization as delineated in Figure 1c, while the dependence of ΔT_{37-19} on CWV is weak. As a consequence, we conclude that combined use of $T_{19V} - T_{10V}$ and $T_{37H} - T_{19H}$ is suitable to retrieve CWV and LWP, taking advantage of their insensitivity to near-surface wind speed and orthogonality with respect to CWV and LWP.

[21] The inversion algorithm is based on a lookup table method, where a set of calculated brightness temperatures is tabulated in seven dimensions including five inputs, i.e., water vapor scale height, sea surface temperature, near-surface wind speed, cloud top temperature, and cloud base temperature. The remaining two dimensions are retrievals, i.e., CWV and LWP, to be determined by Newton-Raphson iteration in terms of $T_{19V} - T_{10V}$ and $T_{37H} - T_{19H}$. To obtain a set of microwave brightness temperatures in forward simulations, the atmospheric temperature is assumed to decrease linearly with increasing altitude at the lapse rate of 6.5 K/km from sea surface temperature as the lower boundary. The cosmic background radiation of 2.7 K incident through the top of the atmosphere is included. The droplet size distribution of clouds is assumed to be the lognormal distribution with the mode radius of 10 μm , but the calculated results are equally applicable to the whole range of variations in the droplet size distributions for nonprecipitating clouds because the brightness temperatures are insensitive to the size distribution in the microwave frequencies considered here. This presumption would be invalid if clouds are associated with heavy rainfall, so that scattering by large raindrops dominates the 37-GHz brightness temperature. The present analysis, however, is focused on low clouds,

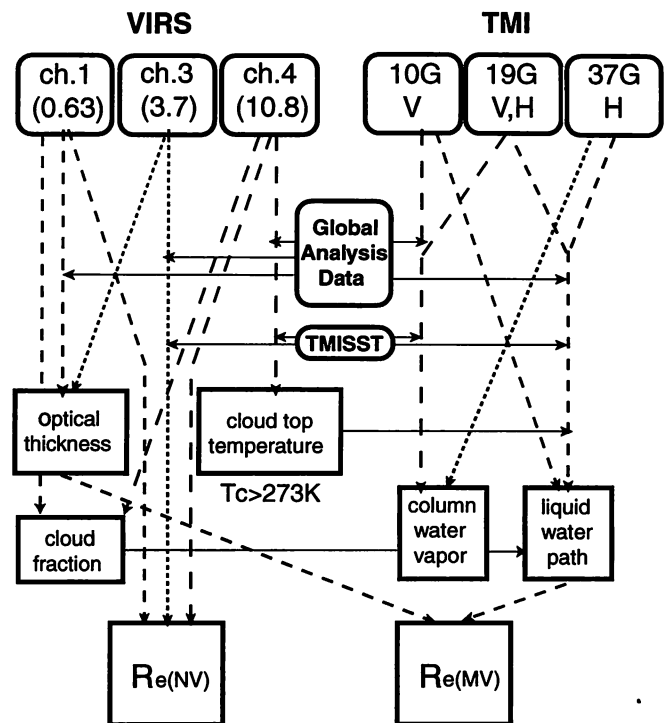


Figure 2. Overall flow of the combined algorithm is illustrated. VIRS and TMI denote the Visible and Infrared Scanner and TRMM Microwave imager, respectively. $R_{e(NV)}$ is the cloud effective radius retrieved from near-infrared and visible radiances, and $R_{e(MV)}$ is that which is retrieved from the microwave and the visible. TMISST as the TMI-retrieved sea surface temperature, which is provided by the Earth Observation Research Center (EORC) of the National Space Development Agency of Japan (NASDA). See section 2.3 for more detail.

which are not precipitating or are associated with warm rain, and in general, warm rain is not frequently so heavy. Note that our radiative transfer code includes multiple scattering and is readily applicable to heavily precipitating clouds as well if precipitating drops are incorporated in the model assumptions.

2.3. Combined Algorithm

[22] Overall flow of the algorithm for combined measurements by VIRS and TMI is outlined in Figure 2. First, we perform VIRS analysis to retrieve the cloud optical thickness, the effective droplet radius, the cloud top temperature, and the cloud fraction (described below in this section). The TMI analysis algorithm is applied to cloudy pixels identified by the VIRS algorithm, with cloud top temperature given by VIRS outputs to specify the cloud top height and water temperature. This procedure eliminates ambiguity in the cloud water temperature (see section 2.4), which would produce large uncertainties in estimation of LWP_{micr} using only microwave channels at frequencies lower than 37 GHz [*Greenwald et al.*, 1993; *Lin et al.*, 1998a]. The cloud base temperature is specified by the atmospheric temperature at the lifting condensation level derived from the objective analysis archives.

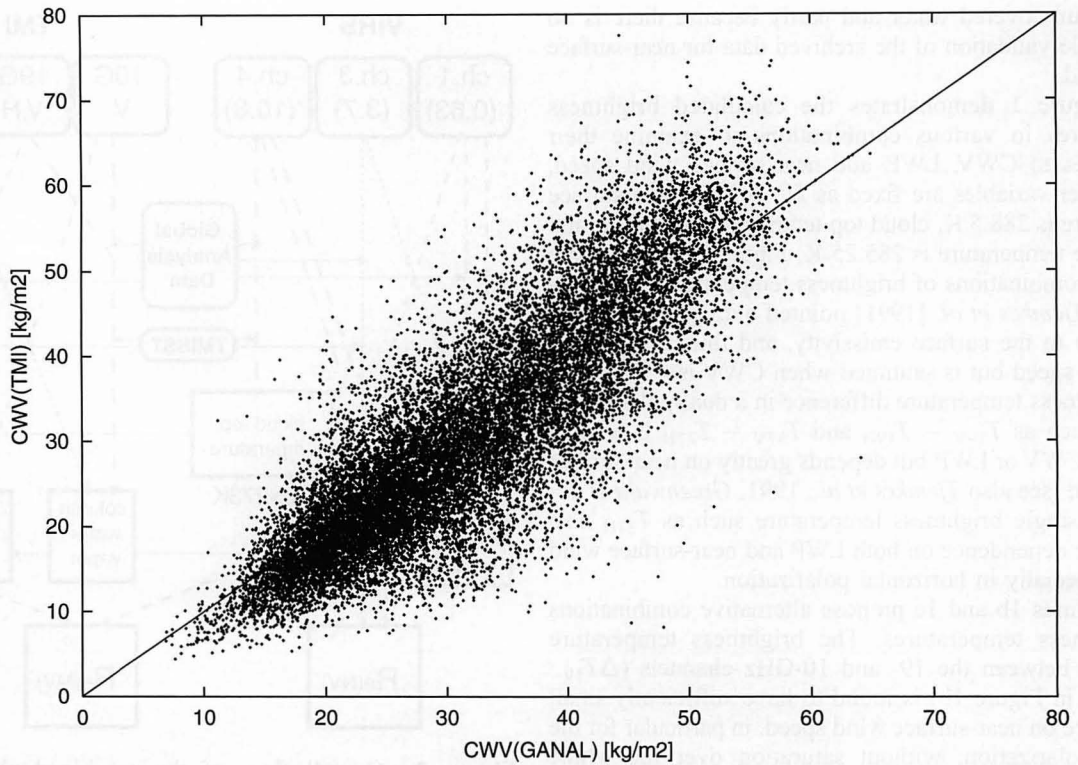


Figure 3. Scatterplot for the TRMM Microwave Imager (TMI)-retrieved CWV (ordinate) versus CWV calculated from global analysis (GANAL) (abscissa).

[23] Cold clouds with the top temperatures <273 K are omitted because we restrict our target to liquid water clouds in the present analysis. Our lack of knowledge in the optical properties of ice crystals, especially in the near infrared, prevents us from precise estimation of the effective radius for ice clouds by remote-sensing technique to date. Ice clouds, moreover, are not detectable by microwave radiometers unless the channel frequency is so large that scattering of ice crystals dominates brightness temperature.

[24] As mentioned in section 1, the beam-filling problem arising from the different spatial resolutions between VIRS and TMI should be properly taken into account before the data matching. In our combined algorithm the cloud fraction f_c is determined by the ratio of the number of cloudy pixels to the total pixel number (9^2) within a VIRS data segment (compare section 3). This cloud fraction is considered as the beam-filling efficiency for LWP_{micr} within the corresponding TMI footprint. The simulated brightness temperatures tabulated in the lookup table are then modified as

$$T_b^{\text{mod}}(\text{LWP}) = f_c T_b^{\text{org}}(\text{LWP}) + (1 - f_c) T_b^{\text{org}}(\text{CS}), \quad (5)$$

where T_b^{mod} and T_b^{org} are modified and original brightness temperatures, respectively, and CS is clear sky. Current retrieval schemes for LWP_{micr} yield an averaged quantity over a footprint without correction of the beam-filling efficiency. Using (5) requires caution when f_c is very small because it could enlarge noise associated with the surface emissivity to severely degrade cloud signals. We therefore exclude the data with $f_c < 1/3$ from analysis. Impact of the

cloud fraction correction on estimation of LWP_{micr} is demonstrated in section 4.

[25] LWP_{micr} in combination with the optical thickness, defines the effective droplet radius $R_{e(MV)}$, i.e.,

$$R_{e(MV)} = \frac{3LWP_{\text{micr}}}{2\rho_w \tau_c}, \quad (6)$$

in the different way from another effective radius estimated from visible and near-infrared measurements $R_{e(NV)}$. *Lin et al.* [1998b] also estimated $R_{e(MV)}$ using τ_c from the ISCCP database, where τ_c is retrieved under the assumption that R_e is constant at $10 \mu\text{m}$. On the other hand, our algorithm yields τ_c and $R_{e(NV)}$ self-consistently by the two-channel method from shortwave measurement (section 2.1). We will discuss an intercomparison of $R_{e(NV)}$ and $R_{e(MV)}$ in section 4.

2.4. Validation and Error Analysis

[26] Here we concentrate the validation study on the microwave retrievals since the shortwave part of our retrieval algorithm has been examined in detail by *Nakajima and Nakajima* [1995]. For validation of CWV we examine the correlation of the microwave-retrieved CWV with the vertically integrated water vapor content taken from global analysis (GANAL) data. On the other hand, ground truth data to validate satellite-retrieved LWP are very limited. Although *Greenwald et al.* [1993] compared ground and shipborne radiometer measurements with satellite retrievals in the use of histograms, sampling errors in LWP are not negligible for more quantitative validation. We therefore do

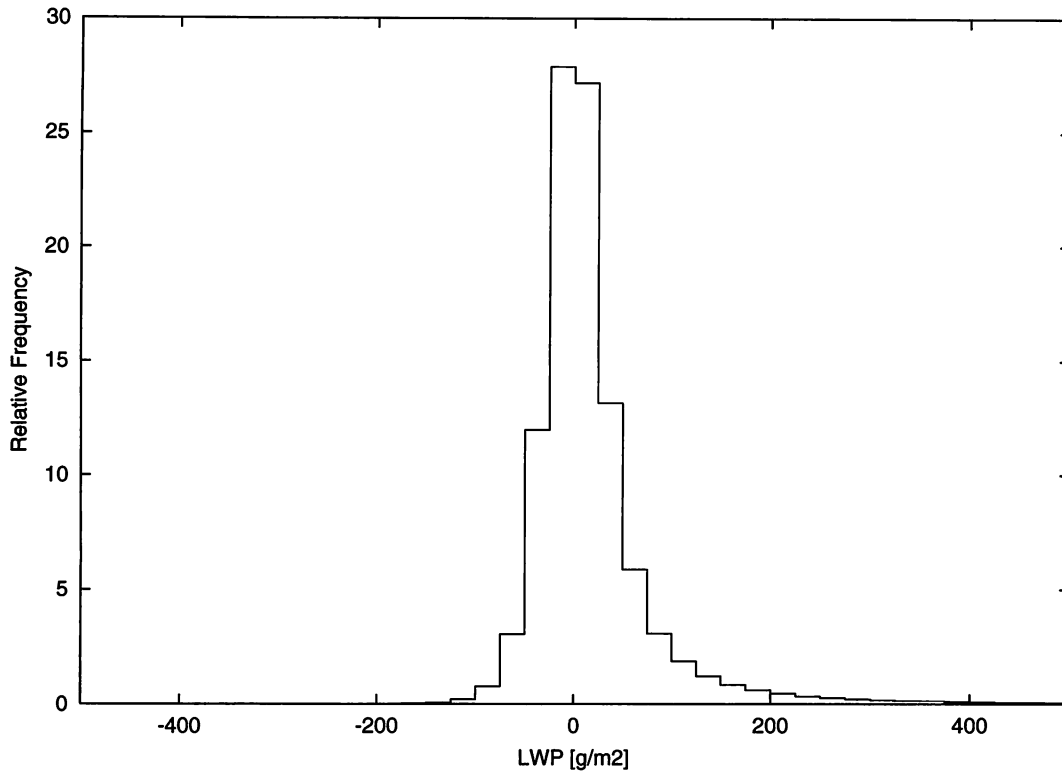


Figure 4. Frequency distribution of microwave-retrieved LWP (LWP_{micr}) for clouds with the optical thickness <3 . The ordinate is the relative frequency in the unit of percent, and the abscissa is LWP_{micr} .

not demonstrate that ground measurement validates LWP, but the frequency distribution of LWP is presented under the nearly clear-sky condition to check if there is any bias in the retrieved LWP_{micr} . Comparison between LWP_{micr} and LWP_{shrt} is performed in section 4 as an interconsistency check of both the LWPs.

[27] Figure 3 shows a scatter diagram for CWV estimated from microwave measurement and GANAL data. TMI-CWV is in reasonable agreement with the GANAL product although data points are scattered around the $y = x$ line, where the RMS error in retrieved CWV is estimated to be 4.8 kg/m^2 . One of the possible reasons for the scatter is contamination of LWP associated with heavy precipitation. Precipitation water would enhance brightness temperatures even in the low-frequency channels, while scattering by large precipitating hydrometeors would influence brightness temperatures in the 37-GHz and higher-frequency channels. In such cases our current algorithm could produce misestimation of CWV and LWP. The water cloud criterion (see section 2.3) saves our retrievals from significant contamination of large frozen hydrometeors. Mismatches in space and time between TMI-CWV and GANAL-CWV would also produce, in part, the scatter in Figure 3 as well as intrinsic errors in GANAL-CWV.

[28] The frequency distribution of LWP_{micr} is shown in Figure 4 under the clear-sky condition in order to check possible bias in estimation of LWP_{micr} according to *Lin and Rossow* [1994]. Retrieved LWP_{micr} might not be exactly zero even in cloud-free areas because of instru-

mental calibration problems and/or ambiguities in the model assumptions as to the surface emissivity. The distribution function of LWP_{micr} under the clear-sky condition is expected to be centered at $LWP = 0$, if no bias exists, with a finite deviation due to the ambiguities. We consider the clear-sky criterion as the regions where the cloud optical thickness is <3 instead of cloud-free areas, in a strict sense, since cloud top temperature is required as an input to our microwave algorithm. Figure 4 shows no significant bias in the peak position of the distribution function. The retrieved LWP_{micr} therefore is assured to suffer from no considerable bias without any artificial adjustment in the algorithm.

[29] We evaluate error sensitivities in estimation of LWP to various sources of uncertainties according to *Greenwald et al.* [1993]. Major sources of errors are incorporated in the error estimation as

$$\begin{aligned} \sigma_{TOT}^2 \approx & \left(\sigma_{SST} \frac{\partial LWP}{\partial SST} \right)^2 + \left(\sigma_{SW} \frac{\partial LWP}{\partial SW} \right)^2 \\ & + \left(\sigma_{T_c} \frac{\partial LWP}{\partial T_c} \right)^2 + \left(\sigma_{T_{cb}} \frac{\partial LWP}{\partial T_{cb}} \right)^2 \\ & + \left(\sigma_{CWV} \frac{\partial LWP}{\partial CWV} \right)^2, \end{aligned} \quad (7)$$

where σ_{SST} , σ_{SW} , σ_{T_c} , $\sigma_{T_{cb}}$, and σ_{CWV} are RMS errors in sea surface temperature, near-surface wind speed, cloud top temperature, cloud base temperature, and CWV, respectively, and σ_{TOT} is the resultant RMS error in LWP.

Table 2. Estimated Errors in Liquid Water Path (LWP) of 50, 100, 150, and 200 g/m² with CWV of 26 and 52 kg/m^{2a}

LWP	SST	WS	T_c	T_{cb}	CWV	Total	Relative Error, %
<i>CWV = 26 kg/m²</i>							
50	1.50	8.78	0.29	2.63	17.45	19.78	39.55
100	1.53	8.95	0.39	3.46	20.78	22.94	22.94
150	1.56	8.96	0.49	4.27	24.26	26.26	17.51
200	1.59	8.81	0.57	5.06	27.92	29.76	14.88
<i>CWV = 52 kg/m²</i>							
50	1.55	9.05	0.50	5.43	3.19	11.15	22.30
100	1.58	8.71	0.59	6.25	6.36	12.58	12.58
150	1.61	8.25	0.68	7.05	9.71	14.66	9.78
200	1.64	7.67	0.75	7.84	13.24	17.29	8.64

^aSee equation (7). Other independent variables are fixed. Water vapor scale height $H_w = 2.3$ km, sea surface temperature SST = 295 K, near-surface wind speed WS = 5 m/s, cloud top temperature $T_c = 275.5$ K, and cloud base temperature $T_{cb} = 285.25$ K.

[30] Derivatives in the right-hand side of (7) are estimated as, for example,

$$\frac{\partial \text{LWP}}{\partial \text{SST}} \approx \left(\frac{\partial \text{LWP}}{\partial \Delta T_{37-19}} \right) \left(\frac{\partial \Delta T_{37-19}}{\partial \text{SST}} \right), \quad (8)$$

where $\Delta T_{37-19} \equiv T_{37H} - T_{19H}$ is supposed here to be exclusively responsible for evaluation of LWP, which is a reasonable approximation to our algorithm (section 2.2).

[31] Results of error analysis are summarized in Table 2. The square root of each term in (7) is tabulated for LWPs of 50, 100, 150, and 200 g/m², which cover majority of nonprecipitating clouds, with CWV of 26 and 52 kg/m². Here we assume that σ_{SST} , σ_{WS} , σ_{T_c} , $\sigma_{T_{cb}}$, and σ_{CWV} are 0.68 K, 2 m/s, 1°, 5°, and 4.8 kg/m² (see section 2.4) in RMS errors, respectively. Although all of these values except σ_{SST} and σ_{CWV} are only crude estimates, they are considered to be plausible representatives. The largest source of error is attributed to CWV for the smaller CWV case, but uncertainty in near-surface wind speed makes a comparable contribution in more moist atmospheres, particularly for small values of LWP. The decreasing tendency of the error due to CWV with increasing CWV is clearly demonstrated in Figure 1c (left) of Figure 1 where $|\partial T_{37-19} / \partial \text{CWV}|$ decreases with increasing CWV to reach ~ 0 for CWV > 40 kg/m² (see equation (8)). Ambiguities in the cloud temperature become significant with increasing LWP as also found by *Greenwald et al.* [1993]. Uncertainties in cloud base temperature are not negligible for large values of LWP under a possibly pessimistic assumption of $\sigma_{T_{cb}} = 5^\circ$. On the other hand, cloud top temperature, determined precisely by VIRS analysis, is found to provide no serious errors. The total error ranges from 20 to 30 g/m² for relatively dry atmospheres, whereas it decreases down to the range 11–18 g/m² for more moist atmospheres.

3. Data

[32] We adopt the TRMM level 1 products (version 5) for VIRS radiances (1B01) and for TMI brightness temperature (1B11). VIRS radiance data are selectively arrayed into data segments, each of which is assigned on the global grid of $0.25^\circ \times 0.25^\circ$, where a segment consists of 9×9

neighboring pixels. TMI brightness temperatures are assigned on the common grid after the uncovered data with the narrower VIRS swath are omitted. Observational time difference measured at a certain ground point caused by difference in the scan geometry between VIRS and TMI, ~ 1 min, is negligibly small.

[33] A VIRS footprint size is 2.1 km, and hence the 9×9 segment covers a 19 km \times 19 km area. On the other hand, the effective field of view (EFOV) of TMI is 63.2 km (down track) \times 9.1 km (cross track) for the 10.65-GHz channel, 30.4 km \times 9.1 km for the 19.35-GHz channel, and 16.0 km \times 9.1 km for the 37.0-GHz channel [*Kummerow et al.*, 1998].

[34] Difference in spatial resolution between VIRS and TMI channels, which can be a factor of 10 or more, could produce large bias when combining the retrievals by these two sensors unless proper correction is made. In our algorithm the cloud fraction correction is made to reduce errors as described in section 2.3.

[35] Discrepancy in spatial resolution between 37- and 19-GHz channels, which are mainly responsible for retrieving LWP, would be significant if observed cloud system has considerable spatial variation in the scale of ~ 30 km (the resolution of 19-GHz channel) or less. The climatological interest, however, in the present series of our study is focused on low clouds, e.g., stratocumulus and stratus, which are typically extended to a much larger scale showing relatively homogeneous features. We therefore consider that the discrepancy between 37- and 19-GHz channels would not cause serious errors in estimation of LWP for our purpose.

[36] Analogous discussion can be made for discrepancy in spatial resolution between 19- and 10-GHz channels, which are mainly responsible for CWV. That is, estimated CWV would not suffer from large errors if water vapor shows no great spatial fluctuation within ~ 60 -km scale (the resolution of 10-GHz channel). In general, this assumption is not severely ruled out.

[37] Our algorithm requires some ancillary data. We adopt the daily mean data of TMI-retrieved sea surface temperature (TMISST) [*Shibata et al.*, 1999; M. Kachi et al., Sea surface temperatures retrieved from TRMM Microwave Imager and Visible Infrared Scanner, submitted to *Journal of the Meteorological Society of Japan*, 2001] for the sea surface temperature for both visible/infrared and microwave analyses. The use of TMISST has some advantages compared with previous studies. In the current algorithms the ground surface temperature has been obtained often by objective analysis archives, infrared radiometric measurement, or climatological data. Objective analysis archives, however, interpolate local meteorological data acquired by ground-based measurements in space and time, and the infrared-retrieved surface temperature is restricted into cloud-free areas. Climatological data do not include regional or temporal variations. Sea surface temperature retrieved by a spaceborne microwave radiometer does not suffer from these difficulties and in particular, TMISST minimizes sampling errors for our TRMM analysis.

[38] The water vapor correction required for the VIRS analysis and the near-surface wind speed and lifting condensation level for the TMI analysis are determined by the GANAL data, which are 6-hourly objective analysis

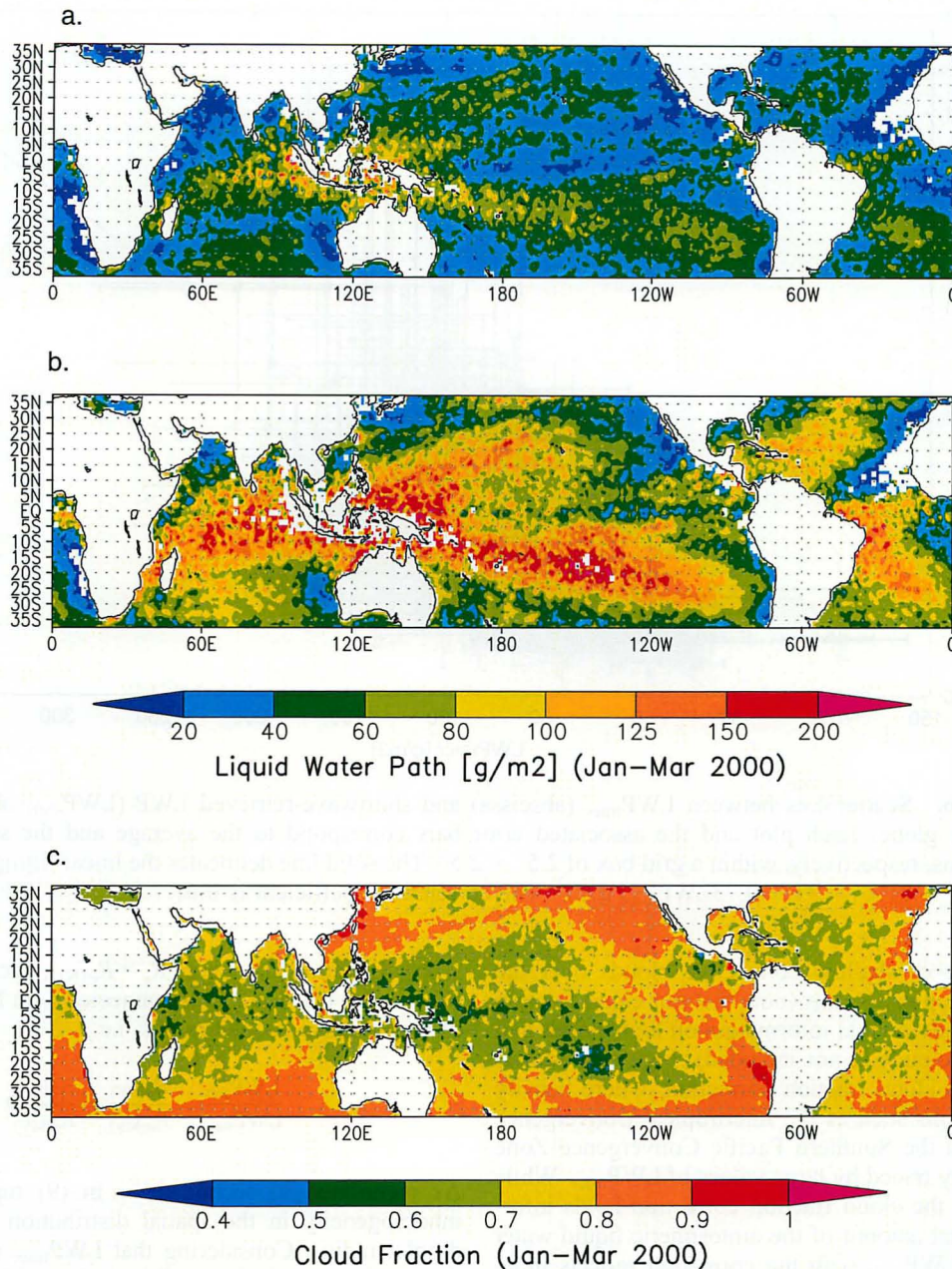


Figure 5. Three-monthly mean LWP_{micr} (a) without the cloud fraction correction, (b) with the correction, and (c) the cloud fraction for January to March 2000.

archives provided by the Japanese Meteorological Agency. The GANAL data, assigned on the $1.25^\circ \times 1.25^\circ$ grid, are linearly interpolated onto the 0.25×0.25 grid for matching satellite data. The CWV estimated from GANAL data is used as well for validation of the TMI-retrieved CWV (section 2.4).

4. Results

[39] In this section we show the results of global analysis to obtain the cloud physical properties, applying the algorithm to TRMM data during January to March 2000. The global distributions of LWP_{micr} in a 3-monthly mean

are illustrated in Figure 5. Figure 5a shows LWP_{micr} derived without the cloud fraction correction (section 2.3), i.e., assuming $f_c = 1$ anywhere for reference. The spatial structure of LWP_{micr} in Figure 5a has been smoothed out within the scale of 16–30 km, which is limited by the resolution of TMI footprints of the 19.35- and 37.0-GHz channels. LWP_{micr} without the cloud fraction correction is comparable with the current definition of LWP derived by microwave measurement, but it could largely underestimate the actual mixing ratio of the cloud liquid water when the cloud fraction is small. The global distribution of the cloud fraction (Figure 5c) has characteristic features, showing small values corresponding to the fre-

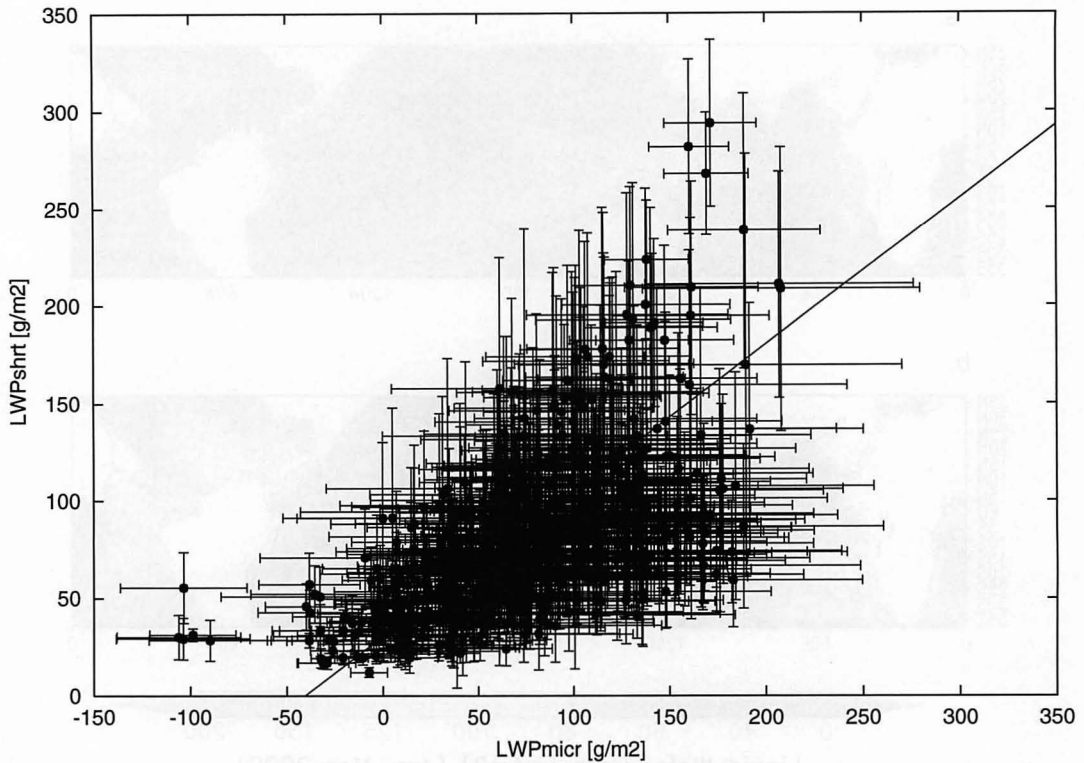


Figure 6. Scatterplots between LWP_{micr} (abscissa) and shortwave-retrieved LWP (LWP_{shrt} ; ordinate) over the globe. Each plot and the associated error bars correspond to the average and the standard deviations, respectively, within a grid box of $2.5^\circ \times 2.5^\circ$. The solid line delineates the linear fitting curve, given by $LWP_{shrt} = 31 + 0.75LWP_{micr} \text{ g/m}^2$. The correlation coefficient is 0.61.

quent appearance of shallow convective clouds over the tropical and subtropical oceans (note that our cloud fraction is that of low clouds, so that information on high clouds and deep convective clouds is not included). Figure 5b shows LWP_{micr} with the cloud fraction correction, where heavily precipitating regions such as the Intertropical Convergence Zone (ITCZ) and the Southern Pacific Convergence Zone (SPCZ) are clearly traced by large values of LWP_{micr} . While LWP_{micr} without the cloud fraction correction holds information on the total amount of the atmospheric liquid water over the globe, LWP_{micr} with the correction reflects more directly the physical properties of individual clouds. In particular, the cloud fraction correction is inevitable for evaluating $R_{e(MV)}$ by (6).

[40] One may wonder at the apparent inverse correlation between cloud fraction and LWP observed in Figure 5. This trend is explained by the fact that shallow convective clouds over the tropical and subtropical oceans account for smaller cloud fractions, whereas coastal stratus and stratocumulus account for larger cloud fractions. Oceanic shallow convective clouds, often associated with warm rain, typically have considerably larger LWP than nonprecipitating stratiform clouds such as stratus and stratocumulus. The inverse correlation therefore reflects the regional variation in low-cloud properties. This tendency, however, could be inverted if some specific types of clouds are of interest. Positive correlation between cloud fraction and LWP was found for stratus clouds [Zuidema and Hartmann, 1995] and for the North Pacific clouds which are dominated by northern midlatitude storms [Greenwald et al., 1995].

[41] Equation (1), where $R_e = R_{e(NV)}$ in combination with (6), implies that LWP_{shrt} is connected with LWP_{micr} in terms of the effective droplet radius, i.e.,

$$\frac{LWP_{shrt}}{LWP_{micr}} = \frac{R_{e(NV)}}{R_{e(MV)}} = \frac{\gamma \langle R_e \rangle}{R_{e(MV)}}. \quad (9)$$

As mentioned in section 1, γ in (9) represents vertical inhomogeneity in the spatial distribution of the effective droplet radius. Considering that LWP_{micr} and τ_c represent the entire physical condition throughout the vertical extent of clouds, we may substitute $\langle R_e \rangle$ by $R_{e(MV)}$ in (9) to find

$$\frac{LWP_{shrt}}{LWP_{micr}} = \frac{R_{e(NV)}}{R_{e(MV)}} = \gamma. \quad (10)$$

[42] Brenguier et al. [2000] showed that $\langle R_e \rangle$ is smaller by the factor of 5/6 than the cloud top value on the basis of the adiabatic model describing the microphysical evolution of a convective closed parcel of moist air. Nakajima and King [1990] demonstrated that $R_{e(NV)}$ approaches to the cloud top value in optically thick clouds, and in this case we may replace γ by 6/5 in (10). Nonprecipitating clouds therefore are expected to show LWP_{shrt} slightly larger than LWP_{micr} . On the other hand, LWP_{shrt} would be exceeded by LWP_{micr} if a large number of cloud droplets grow to raindrops and disappear from the cloud top as they fall down to below the cloud base since raindrops

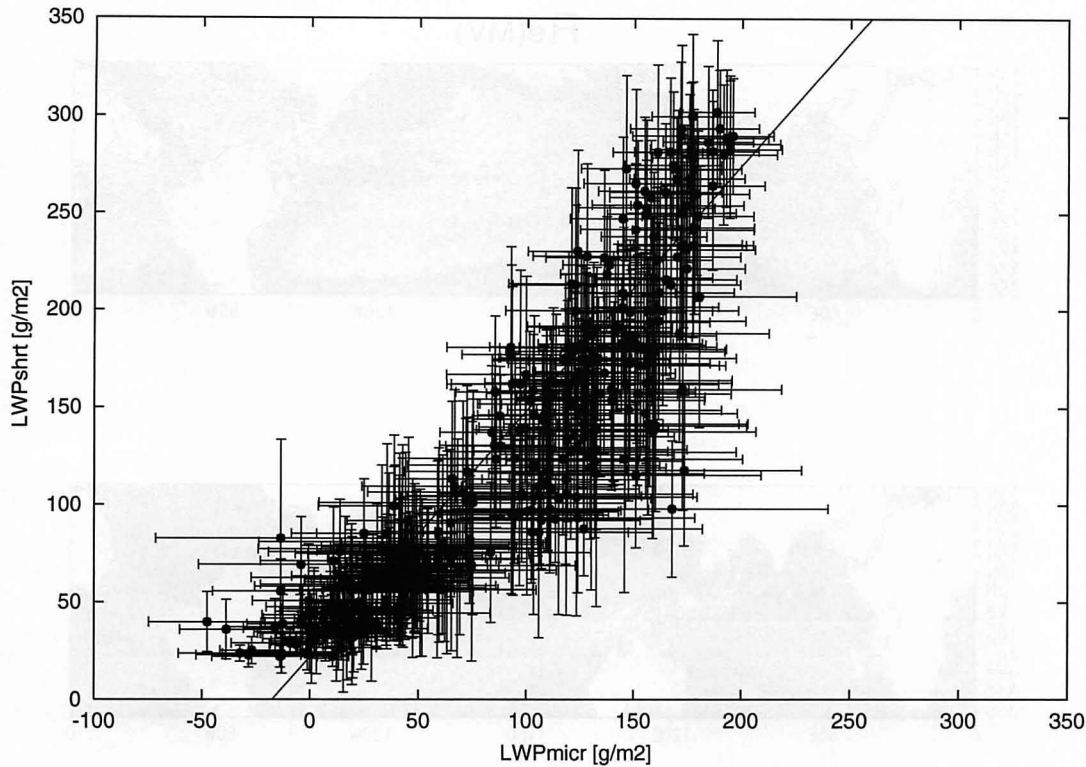


Figure 7. Same as Figure 6, but with the target area a rectangular region of 15°S – 30°S and 75°W – 85°W in western Chile. The linear fitting curve is given by $\text{LWP}_{\text{shrt}} = 22 + 1.26 \text{LWP}_{\text{micr}}$ (g/m^2) with a correlation coefficient of 0.91.

below a cloud layer are detectable for microwave measurement but not for shortwave.

[43] The scatter diagram of LWP_{shrt} versus LWP_{micr} over the globe is shown in Figure 6, where each plot and the associated error bars correspond to the average and the standard deviations, respectively, within a grid box of $2.5^{\circ} \times 2.5^{\circ}$. The linear fitting curve is given by $\text{LWP}_{\text{shrt}} = 31 + 0.75\text{LWP}_{\text{micr}}$ g/m^2 , and the correlation coefficient between LWP_{shrt} and LWP_{micr} is 0.62. One finds that data plots are largely scattered around the fitting curve, the slope of which (0.75) is considerably smaller than $6/5$. This implies that such clouds as represented by the adiabatic model, e.g., nonprecipitating cumuli, are contaminated by other types of clouds having LWP_{micr} larger than LWP_{shrt} . A plausible interpretation is that Figure 6 includes precipitating clouds along with nonprecipitating ones.

[44] Figure 7 is same as Figure 6 but only in a rectangular area of 15°S – 30°S and 75°W – 85°W in western Chile, where stratus clouds in the boundary layer are frequently observed. The linear fitting curve for Figure 7 is given by $\text{LWP}_{\text{shrt}} = 22 + 1.26\text{LWP}_{\text{micr}}$ g/m^2 with the correlation coefficient of 0.91, which indicates that the adiabatic model is a much better representative of low clouds in this area than in the global average (Figure 6). This result is consistent with the fact that clouds in this area rarely provide heavy rainfall.

[45] The global trend of both $R_{e(\text{NV})}$ and $R_{e(\text{MV})}$ is presented in Figure 8 (top). In the upper panel, $R_{e(\text{MV})}$ in the tropics and subtropics shows very large values exceeding $50 \mu\text{m}$, which are considered as the contribution of

raindrops. Surrounding areas, on the contrary, show much smaller $R_{e(\text{MV})}$ below $10 \mu\text{m}$. Areas with large $R_{e(\text{NV})}$ also trace precipitating regions (Figure 8, bottom) but are less pronounced than for $R_{e(\text{MV})}$. Careful examination of Figure 8 reveals that $R_{e(\text{MV})}$ is smaller than $R_{e(\text{NV})}$, i.e., $R_{e(\text{NV})}/R_{e(\text{MV})} = \gamma > 1$, in the areas with little precipitation, such as western California, Chile, and southern Africa.

[46] A probable implication inferred from these results is summarized as follows. Characteristic difference between LWP_{shrt} and LWP_{micr} closely reflects vertical inhomogeneity of the effective droplet radius within or below a cloud layer, which causes discrepancy between $R_{e(\text{NV})}$ and $R_{e(\text{MV})}$. Clouds with LWP_{shrt} larger than LWP_{micr} (or $R_{e(\text{NV})}$ larger than $R_{e(\text{MV})}$) are not precipitating. In contrast, clouds are expected to be associated with rainfall if LWP_{shrt} (or $R_{e(\text{NV})}$) is significantly smaller than LWP_{micr} (or $R_{e(\text{MV})}$). Furthermore, the intermediate stage, at which clouds are drizzling near the cloud top but are not producing considerable amount of raindrops, would be identified as well by closer examination of $R_{e(\text{NV})}$ and $R_{e(\text{MV})}$.

[47] We therefore presume that the relation between LWP_{shrt} and LWP_{micr} , or more directly, between $R_{e(\text{MV})}$ and $R_{e(\text{NV})}$, reflects a microphysical mechanism to expedite or suppress the conversion of the cloud water into rainfall. X. Masunaga et al. (Physical properties of maritime low clouds as retrieved by combined use of Tropical Rainfall Measurement Mission Microwave Imager and Visible/Infrared Scanner, 2, Warm clouds and rain, submitted to *Journal of Geophysical Research*, 2001) will investigate the microphysical evolution of low clouds in

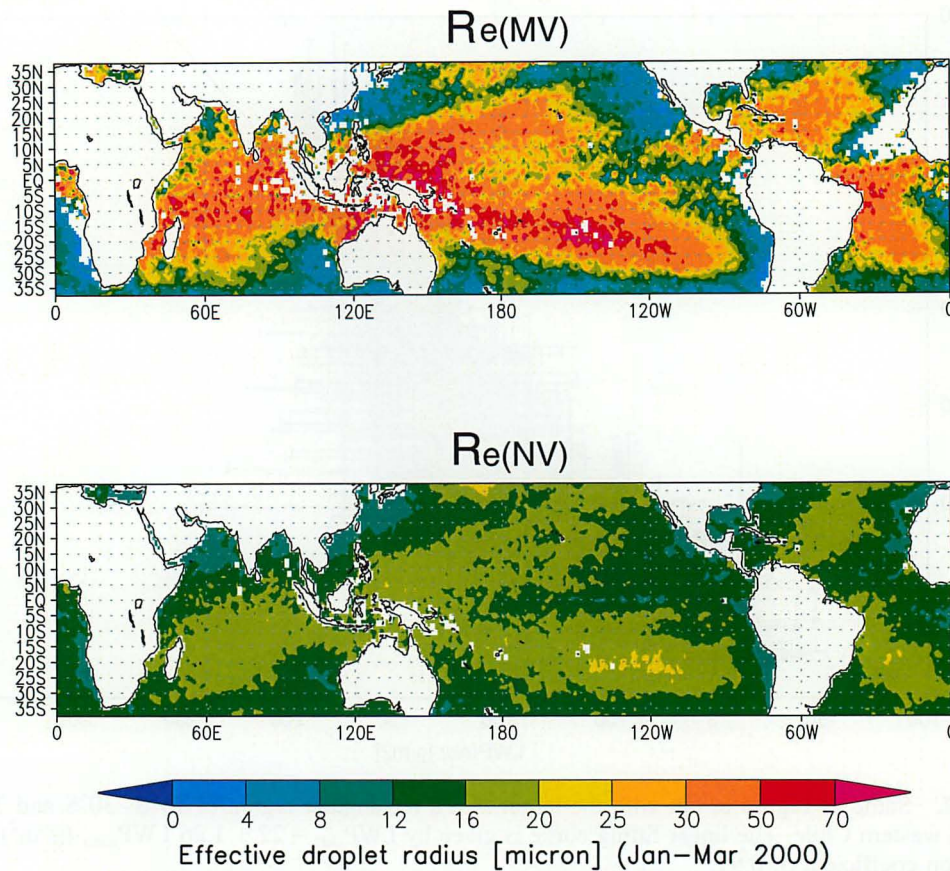


Figure 8. Three-monthly mean (top) $R_{e(MV)}$ and (bottom) $R_{e(NV)}$ for January to March 2000.

terms of the relation and difference between $R_{e(MV)}$ and $R_{e(NV)}$, along with other possible interpretations such as nonadiabaticity of clouds.

5. Summary

[48] In this paper a physical inversion algorithm is presented in the combined use of visible/infrared and microwave sensors to retrieve the cloud physical quantities such as LWP and the effective droplet radius. LWP is defined in two separate ways: where shortwave measurement yields LWP_{shrt} according to (1) and the microwave retrieval directly provides LWP_{micr} . Correspondingly, $R_{e(MV)}$ is determined by (6) in a different way from the shortwave-retrieved effective radius $R_{e(NV)}$.

[49] Our current algorithm is based on the sensor specifications of VIRS and TMI aboard the TRMM satellite. To analyze VIRS measurements, we follow a two-channel method as incorporated in the GLI algorithm, which was originally developed by *Nakajima and Nakajima* [1995] and *Kawamoto et al.* [2001]. The retrieval method for TMI measurement makes combined use of $T_{19V} - T_{10V}$ and $T_{37H} - T_{19H}$ to evaluate CWV and LWP by means of a lookup table based on radiative transfer simulations performed under a set of the free parameters of sea surface temperature, near-surface wind speed, cloud top temperature, and cloud base temperature. The cloud top temperature required for the TMI analysis is taken

from the VIRS retrieval, which substantially reduces uncertainties in estimation of LWP. Total errors in estimation of LWP are within $11\text{--}30\text{ g/m}^2$ for realistic ranges of LWP and CWV. The beam-filling efficiency of clouds for the TMI footprints is corrected by the cloud fraction evaluated from the VIRS measurements.

[50] For application, global analysis is performed with 3-monthly data from January to March 2000. The cloud fraction correction is demonstrated to have a large impact on estimation of LWP_{micr} in particular, in the low-latitude regions (Figure 5).

[51] The scatter diagram of LWP_{shrt} versus LWP_{micr} for clouds in western Chili, which are typically nonprecipitating stratus clouds, shows a high linear correlation with the slope of the fitting curve of $\approx 6/5$. This is explained, through the close relation between the LWPs and the effective radii (10), by the vertical inhomogeneity of droplet size in a cloud layer, as derived by *Brenguier et al.* [2000] on the basis of the adiabatic cloud model. In contrast, the fitting curve has the slope $< 6/5$ for the global average with worse correlation mainly because of contamination of clouds with LWP_{micr} larger than LWP_{shrt} . Precipitating clouds account for this excess of LWP_{micr} over LWP_{shrt} due to the presence of raindrops below the cloud base.

[52] These tendencies are more widely recognized by examination of the global distributions of $R_{e(MV)}$ and $R_{e(NV)}$, where $R_{e(MV)}$ largely exceeds $R_{e(NV)}$ in precipitating regions such as ITCZ and SPCZ, but the relation is

inverted in the areas with little precipitation, e.g., western California, Chile, and southern Africa. The result implies that the difference between $R_{e(MV)}$ and $R_{e(NV)}$ reflects a microphysical mechanism to expedite or suppress the conversion of the cloud water into rainfall. X. Masunaga et al. (manuscript in preparation, 2001) will be dedicated to clarify the origin of the discrepancy between $R_{e(MV)}$ and $R_{e(NV)}$, along with other possible interpretations such as nonadiabicity of clouds.

[53] **Acknowledgments.** The authors are grateful to the anonymous referees for helpful comments, which have improved the manuscript. VIRS and TMI data were provided by NASA Goddard Space Flight Center. Japan Meteorological Agency provided GANAL data. TMSST (version 2.0) was produced and supplied by NASDA/Earth Observation Research Center.

References

- Brenguier, J.-L., H. Pawlowska, L. Schüller, R. Preusker, J. Fischer, and Y. Fouquart, Radiative properties of boundary layer clouds: Droplet effective radius versus number concentration, *J. Atmos. Sci.*, *57*, 803–821, 2000.
- Chang, A. T. C., and T. T. Wilheit, Remote sensing of atmospheric water vapor, liquid water, and wind speed at the ocean surface by passive microwave techniques from the Nimbus 5 satellite, *Radio Sci.*, *14*, 793–802, 1979.
- Greenwald, T. J., G. L. Stephens, T. H. Vonder Haar, and D. L. Jackson, A physical retrieval of cloud liquid water over the global oceans using Special Sensor Microwave/Imager (SSM/I) observations, *J. Geophys. Res.*, *98*, 18,471–18,488, 1993.
- Greenwald, T. J., G. L. Stephens, S. A. Christopher, and T. H. Vonder Haar, Observations of the global characteristics and regional radiative effects of marine cloud liquid water, *J. Clim.*, *8*, 2928–2946, 1995.
- Han, Q., W. B. Rossow, and A. A. Lacis, Near-global survey of effective droplet radii in liquid water cloud using ISCCP data, *J. Clim.*, *7*, 465–497, 1994.
- Kawamoto, K., T. Nakajima, and T. Y. Nakajima, A global determination of cloud microphysics with AVHRR remote sensing, *J. Clim.*, *14*, 2054–2068, 2001.
- Kummerow, C., W. Barnes, T. Kozu, J. Shiue, and J. Simpson, The Tropical Rainfall Measuring Mission (TRMM) sensor package, *J. Atmos. Oceanic Technol.*, *15*, 809–817, 1998.
- Liebe, H. J., and Layton D.H., Millimetre-wave properties of the atmosphere: Laboratory studies and propagation modeling, *Rep. 87-224*, 80 pp., Natl. Telecommun. and Inf. Admin., Washington, D. C., 1987.
- Lin, B., and W. B. Rossow, Observations of cloud liquid water path over oceans: Optical and microwave remote sensing methods, *J. Geophys. Res.*, *99*, 20,907–20,927, 1994.
- Lin, B., B. Wielicki, P. Minnis, and W. Rossow, Estimation of water cloud properties from satellite microwave, infrared, and visible measurements in oceanic environments, 1, Microwave brightness temperature simulations, *J. Geophys. Res.*, *103*, 3873–3886, 1998a.
- Lin, B., P. Minnis, B. Wielicki, D. R. Doelling, R. Palikonda, D. F. Young, and T. Uttal, Estimation of water cloud properties from satellite micro- wave, infrared, and visible measurements in oceanic environments, 2, Results, *J. Geophys. Res.*, *103*, 3887–3905, 1998b.
- Lojou, J.-Y., R. Frouin, and R. Bernard, Comparison of Nimbus-7 SMMR and GOES-1 VISSR atmospheric liquid water content, *J. Appl. Meteorol.*, *30*, 187–198, 1991.
- Nakajima, T., and M. D. King, Determination of the optical thickness and effective particle radius of clouds reflected solar radiation measurements, part I, Theory, *J. Atmos. Sci.*, *47*, 1878–1893, 1990.
- Nakajima, T. Y., and T. Nakajima, Wide-area determination of cloud microphysical properties from NOAA AVHRR measurements for FIRE and ASTEX regions, *J. Atmos. Sci.*, *52*, 4043–4059, 1995.
- Nakajima, T., and M. Tanaka, Effect of wind-generated waves on the transfer of solar radiation in the atmosphere-ocean system, *J. Quant. Spectros. Radiat. Transfer*, *29*, 521–537, 1983.
- Nakajima, T., and M. Tanaka, Matrix formulations for the transfer of solar radiation in a plane-parallel scattering atmosphere, *J. Quant. Spectros. Radiat. Transfer*, *35*, 13–21, 1986.
- Nakajima, T., and M. Tanaka, Algorithms for radiative intensity calculations in moderately thick atmospheres using a truncation approximation, *J. Quant. Spectros. Radiat. Transfer*, *40*, 51–69, 1988.
- Petty, G. W., On the response of the Special Sensor Microwave/Imager (SSM/I) to the marine environment—Implications for atmospheric parameter retrievals, Ph.D. dissertation, 291 pp., Univ. of Wash., Seattle, 1990.
- Prabhakara, C., H. D. Chang, and A. T. C. Chang, Remote sensing of precipitable water over the oceans from Nimbus-7 microwave measurements, *J. Appl. Meteorol.*, *21*, 59–68, 1982.
- Shibata, A., K. Imaoka, M. Kachi, and H. Murakami, SST observation by TRMM Microwave Imager aboard Tropical Rainfall Measuring Mission (in Japanese), *Umi Kenkyu*, *8*, 135–139, 1999.
- Stamnes, K., S.-C. Tsay, W. Wiscombe, and K. Jayaweera, Numerically stable algorithm for discrete-ordinate-method radiative transfer in multiple scattering and emitting layered media, *Appl. Opt.*, *27*, 2502–2509, 1988.
- Takeda, T., and G. Liu, Estimation of atmospheric liquid-water amount by Nimbus 7 SSMR data: A new method and its application to the western North-Pacific region, *J. Meteorol. Soc. Jpn.*, *65*, 931–947, 1987.
- Tjemkes, S. A., G. L. Stephens, and D. L. Jackson, Spaceborne observation of columnar water vapor: SSM/I observations and algorithm, *J. Geophys. Res.*, *96*, 10,941–10,954, 1991.
- Wentz, F. J., and T. Meissner, Algorithm Theoretical Basis Document Version 2: AMSR Ocean Algorithm, *RSS Tech. Proposal 121599A*, 58 pp., Remote Sens. Sys., Santa Rosa, 1999.
- Wilheit, T. T., and A. T. C. Chang, An algorithm for retrieval of ocean surface and atmospheric parameters from the observations of the scanning multichannel microwave radiometer, *Radio Sci.*, *15*, 525–544, 1980.
- Zuidema, P., and D. L. Hartmann, Satellite determination of stratus cloud microphysical properties, *J. Clim.*, *8*, 1638–1657, 1995.

M. Kachi, H. Masunaga, T. Y. Nakajima, and R. Oki, Earth Observation Research Center/NASDA, Harumi Island Triton Square, Office Tower X 22F, 1-8-10 Harumi, Chuo-ku, Tokyo 104-6023, Japan. (kachi@eorc.nasda.go.jp; masunaga@eorc.nasda.go.jp; nakajima@eorc.nasda.go.jp; oki.riko@nasda.go.jp)

S. Kuroda, Sun Microsystems, Inc., 4-10-1 Yoga, Setagaya-ku, Tokyo 158-8633, Japan. (shunsuke.kuroda@sun.co.jp)

T. Nakajima, Center for Climate System Research, University of Tokyo, 4-6-1 Komaba, Meguro-ku, Tokyo 153-8904, Japan. (teruyuki@ccsr.u-tokyo.ac.jp)